

# An Efficient MRF Embedded Level Set Method for Image Segmentation

Xi Yang, Xinbo Gao, *Senior Member, IEEE*, Dacheng Tao, *Senior Member, IEEE*,  
Xuelong Li, *Fellow, IEEE*, and Jie Li

**Abstract**—This paper presents a fast and robust level set method for image segmentation. To enhance the robustness against noise, we embed a Markov random field (MRF) energy function to the conventional level set energy function. This MRF energy function builds the correlation of a pixel with its neighbors and encourages them to fall into the same region. To obtain a fast implementation of the MRF embedded level set model, we explore algebraic multigrid (AMG) and sparse field method (SFM) to increase the time step and decrease the computation domain, respectively. Both AMG and SFM can be conducted in a parallel fashion, which facilitates the processing of our method for big image databases. By comparing the proposed fast and robust level set method with the standard level set method and its popular variants on noisy synthetic images, synthetic aperture radar (SAR) images, medical images, and natural images, we comprehensively demonstrate the new method is robust against various kinds of noises. In particular, the new level set method can segment an image of size  $500 \times 500$  within 3 s on MATLAB R2010b installed in a computer with 3.30-GHz CPU and 4-GB memory.

**Index Terms**—Level set, Markov random field, algebraic multigrid, sparse field method.

Manuscript received August 4, 2013; revised March 5, 2014 and August 9, 2014; accepted November 10, 2014. Date of publication November 20, 2014; date of current version December 8, 2014. This work was supported in part by the National Natural Science Foundation of China under Grant 61125204, Grant 61125106, Grant 61432014, Grant 61172146, and Grant 41031064, in part by the Australian Research Council under Project DP-140102164, Project FT-130101457, and Project LP-140100569, in part by the Fundamental Research Funds for the Central Universities under Grant K5051202048, Grant BDZ021403, and Grant JB149901, in part by Microsoft Research Asia under Project FY13-RES-OPP-034, in part by the Program for Changjiang Scholars and Innovative Research Team in University of China under Grant IRT13088, in part by the Shaanxi Innovative Research Team for Key Science and Technology under Grant 2012KCT-02, and in part the Key Research Program of the Chinese Academy of Sciences under Grant KGZD-EW-T03. The associate editor coordinating the review of this manuscript and approving it for publication was Prof. Jean-Philippe Thiran.

X. Yang and X. Gao are with the State Key Laboratory of Integrated Services Networks, School of Electronic Engineering, Xidian University, Xi'an 710071, China (e-mail: xi.yang.xidian@gmail.com; xbgao@mail.xidian.edu.cn).

D. Tao is with the Centre for Quantum Computation & Intelligent Systems and the Faculty of Engineering and Information Technology, University of Technology, Sydney, 235 Jones Street, Ultimo, NSW 2007, Australia (e-mail: dacheng.tao@uts.edu.au).

X. Li is with the Center for OPTical IMagery Analysis and Learning (OPTIMAL), State Key Laboratory of Transient Optics and Photonics, Xi'an Institute of Optics and Precision Mechanics, Chinese Academy of Sciences, Xi'an 710119, China (e-mail: xuelong\_li@opt.ac.cn).

J. Li is with the Video and Image Processing System Laboratory, School of Electronic Engineering, Xidian University, Xi'an 710071, China (e-mail: leejie@mail.xidian.edu.cn).

Color versions of one or more of the figures in this paper are available online at <http://ieeexplore.ieee.org>.

Digital Object Identifier 10.1109/TIP.2014.2372615

## I. INTRODUCTION

IMAGE segmentation is of great significance in computer vision. Various methods [1], [2] have been proposed to solve this problem, and active contour models in particular have been widely used because they are able to provide smooth and closed boundary contours as segmentation results.

Level set [3] is an implicit representation of active contours. Compared to explicit active contour models [4], [5] which utilize parametric equations to represent evolving contours, level set methods represent the evolving contours as the zero level set of a higher dimensional function, thus making them numerically stable and easily able to handle topological changes.

Existing level set methods for image segmentation can be grouped into two categories: edge-based models [6]–[13] and region-based models [14]–[18].

The *edge-based models* design a stop function with the use of image gradient flow and put the active contour approaching to the object boundary. The geodesic active contour (GAC) model [6], [7] proposed by Caselles *et al.* is one of the most popular models, and its segmentation is driven by the intrinsic geometric measures of images. Li *et al.* [8] presented a variational formulation with an energy term penalizing the deviation of the level set function from the signed distance function, thus completely eliminating the need for costly re-initialization procedure. Recently, a decoupled active contour (DAC) model [9] was presented to speed up the convergence of segmentation by applying the internal and external energy terms separately. The *region-based models* exploit region descriptors to guide the motion of an active contour. The Chan-Vese (CV) model [14] which was proposed on the basis of the Mumford-Shah functional [19], can segment an image into intensity homogeneous regions. Li *et al.* [15] solved the problem of segmenting images with intensity inhomogeneity by using a local binary fitting (LBF) energy. By minimizing the unbiased pixel-wise average misclassification probability (AMP), Wu *et al.* [16] formulated an active contour to segment an image without any prior information about the intensity distribution of regions. By realizing curve evolution via simple operations between two linked lists, Shi and Karl [17] achieved a fast level set algorithm for real-time tracking. Also, they incorporated the smoothness regularization with the use of a Gaussian filtering process and proposed the two-cycle fast (TCF) algorithm to speed up the level set evolution.

Recently, new approaches [20]–[22] have been developed to replace the level set model, which investigate effective optimization schemes [23]. Generally, the level set model minimizes a certain energy function via the gradient descent [24], making the segmentation results prone to getting stuck in local minima. To conquer this problem, Chan *et al.* [25] restated the traditional Mumford-Shah image segmentation model [19] as a convex minimization problem to obtain the global minimum (GM). Another two-stage (TS) image segmentation method [26] solves this problem by firstly finding the unique smooth solution to a convex variant of the Mumford-Shah model, and then using a thresholding strategy to segment the image. Tai *et al.* [27] proposed a graph cut (GC) based optimization method to solve the Mumford-Shah functional and thus improved the segmentation efficiency.

The above methods have obtained promising performance in segmenting high quality images. However, when attempts are made to segment images with heavy noise, the images are easily contaminated, which leads to poor segmentation results. Existing methods assume that pixels in each region are independent when calculating the energy function. This underlying assumption makes the contour motion sensitive to noise. In addition, the implementation of level set methods is complex and time consuming, which limits their application to large scale image databases [28], [29]. To maintain numerical stability, the numerical scheme used in level set methods, such as the upwind scheme or finite difference scheme, must satisfy the Courant-Friedrichs-Lowy (CFL) condition [30], which limits the length of the time step in each iteration and wastes time. The computation of most current level set methods is carried out on a full image domain; however, the calculation of pixels far away from the evolving contour is meaningless for obtaining the object boundary and leads to increased computational complexity.

To address the aforementioned problems, this paper presents a novel level set method for fast and robust image segmentation. The proposed method assumes that the energy function of a pixel is defined by the pixel and its neighbors. By exploiting an MRF model [31] to build an energy function and embedding this energy function into the conventional level set energy function, the adjacent pixels are encouraged to fall into the same region and thus make the segmentation robust to noise. In contrast to the existing implementation of the level set methods, we utilize AMG [32] to increase the time step and decrease the number of iterations, and SFM [33] to constrict the computation of level set function to a narrow band. The integration of AMG and SFM significantly reduces the computational costs. The new level set method can segment an image of size 500 by 500 within three seconds on MATLAB R2010b installed in a computer with 3.30GHz CPU and 4GB memory.

## II. LEVEL SET METHOD

Level set methods implicitly model the planar closed curve  $C$  by the zero level set of the level set function  $\phi(x, y, t)$ , i.e.,

$$C(t) = \{(x, y) | \phi(x, y, t) = 0\}. \quad (1)$$

The level set equation representing the evolution of  $\phi(x, y, t)$  can be written as

$$\frac{\partial \phi}{\partial t} + F |\nabla \phi| = 0, \quad (2)$$

where  $\nabla$  is the gradient operator, and  $F$  denotes the speed of the evolution.

Variational level set methods treat the evolution of the level set equation as a problem of minimizing a certain energy function defined on the level set function  $\phi$ , i.e.,

$$\frac{\partial \phi}{\partial t} = -\frac{\partial E}{\partial \phi}. \quad (3)$$

By using a different energy term to represent certain information, the evolving contour can thus change flexibly according to varying purposes. Thus, variational level set methods are convenient for developing new models for segmentation and have received intensive attentions in recent years.

We can classify existing level set methods into two groups: edge-based models and region-based models.

The *edge-based models* endow  $F$  with specific expression formula. For example, Caselles *et al.* [6] proposed the geodesic active contour (GAC) model

$$\frac{\partial \phi}{\partial t} = |\nabla \phi| \operatorname{div} g \left( \frac{\nabla \phi}{|\nabla \phi|} \right) + v g |\nabla \phi|, \quad (4)$$

where  $\operatorname{div}$  is the divergence operator,  $v$  is a constant coefficient, and  $g$  is the edge stop function defined by

$$g = \frac{1}{1 + |\nabla G_\sigma * I|^2}, \quad (5)$$

and  $G_\sigma$  is the Gaussian kernel with standard deviation  $\sigma$ .

The *region-based models* take the region information into account. For example, the CV model [14] builds the energy function in the frame of the Mumford-Shah functional [19] for segmentation,

$$\begin{aligned} E^{CV}(c_1, c_2, C) = & v \cdot \operatorname{Length}(C) \\ & + \lambda_1 \int_{in(C)} |I(x, y) - c_1|^2 dx dy \\ & + \lambda_2 \int_{out(C)} |I(x, y) - c_2|^2 dx dy, \end{aligned} \quad (6)$$

where  $in(C)$  and  $out(C)$  represent the region inside and outside of the contour  $C$ , respectively.  $c_1$  and  $c_2$  are two constants that represent the approximation of image intensity in  $in(C)$  and  $out(C)$ , respectively.

The upwind scheme and the finite difference scheme are popularly used in level set methods for numerical implementation. Both schemes must satisfy the CFL condition [30], which limits the length of the time step in each iteration, and thus converge slowly.

For example, in the finite difference scheme [8], the level set equation can be discretized as

$$\phi_{i,j}^{k+1} = \phi_{i,j}^k + \Delta t R(\phi_{i,j}^k), \quad (7)$$

where  $(i, j)$  is the spatial index,  $k$  is the temporal index,  $\Delta t$  is the time step, and  $R(\phi_{i,j}^k)$  is the approximation of the right hand side in the evolution equation (4). To maintain

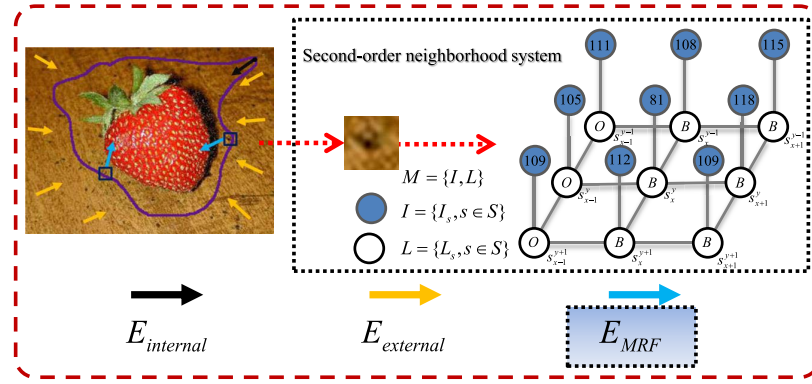


Fig. 1. The proposed energy function framework.

numerical stability and obtain accurate approximation results, CFL condition [30] constraints the length of  $\Delta t$  to a very small one

$$\alpha \Delta t < h^2/4, \quad (8)$$

where  $\alpha$  is one of the coefficient in level set equation, and  $h$  is the grid size.

A small time step  $\Delta t$  increases the number of iterations to convergence, and the full domain computation requires heavy calculations in each iteration. For an image with  $N$  pixels,  $T/\Delta t \propto 4D^2/h^2 = O(N)$  iterations are needed to converge, where  $T$  is the runtime which is in direct proportional to the square of the moved distance  $D$ . For each iteration, the computation is carried out on all the  $N$  pixels, and the cost is  $O(N)$ . Thus, the total computational complexity is  $O(N^2)$ .

### III. MRF EMBEDDED LEVEL SET MODEL

Traditional level set methods ignore the correlation between neighboring pixels, thus making them easy to stop their zero level set curves at a noise point and leading to inaccurate segmentation. To improve the robustness against noise in level set methods, we propose the MRF energy function which builds relationships between pixels and their neighbors.

In general, image segmentation based on level set methods can be viewed as a procedure which a contour is evolved to the object boundary by minimizing a certain energy function.

Similar to popular level set method, the proposed model builds an energy function framework as

$$E = E_{internal} + E_{external} + E_{MRF}. \quad (9)$$

It consists of three terms corresponding to internal energy function, external energy function and MRF energy function, respectively. The internal energy function is defined by characteristics of the evolving contour itself, such as its curvature, length and area. The external energy function concerns the evolution force determined by image information which has no association with the evolving contour, such as the last two terms of the right hand side in (6). The MRF energy function proposed in this paper is added to the energy function framework to reflect the relationship between pixels and their neighbors. Fig. 1 shows the proposed energy function framework.

The MRF energy function constructs a  $(2w+1) \times (2w+1)$  square neighborhood system  $\mathbb{N}^w(s)$ , where sites  $s \in S$  refer to each component of the random variable. Fig. 1 gives a second-order neighborhood system  $\mathbb{N}^1(s)$  ( $w=1$ ), where the eight neighborhood of  $s_x^y$  is defined by

$$\mathbb{N}^1(s) = \{s_{x-1}^{y-1}, s_x^{y-1}, s_{x+1}^{y-1}, s_{x-1}^y, s_{x+1}^y, s_{x-1}^{y+1}, s_x^{y+1}, s_{x+1}^{y+1}\}. \quad (10)$$

A coupled random field is denoted by  $M = \{I, L\}$ , in which  $I = \{I_s, s \in S\}$  is the field of image intensity, and  $L = \{L_s, s \in S\}$  is the label field that separates the object ( $O$ ) from the background ( $B$ ).

The MRF energy function finds the best segmentation label for each pixel with the information of its neighborhood. Normally, this purpose can be realized by maximizing *a posteriori* (MAP) segmentation probability  $P(L|I)$ , which can be obtained with the use of Bayes theorem, i.e.,

$$P(L|I) = \frac{P(I|L)P(L)}{P(I)}. \quad (11)$$

Because  $P(I)$  is a constant that defined by the image itself, the segmentation probability  $P(L|I)$  is proportional to the prior segmentation probability  $P(L)$  and conditional segmentation probability  $P(I|L)$ , i.e.,

$$P(L|I) \propto P(L)P(I|L). \quad (12)$$

Generally, current level set methods assume that pixels in the object region and background region are independent of each other. However, this assumption makes the segmentation result easily disturbed by noise. Therefore, we adopt the MRF theory [31] to construct the formula of  $P(I|L)$  and  $P(L)$ , that is, taking the neighboring relationships into account and defining  $P(I|L)$  and  $P(L)$  of each pixel only depending on its neighborhood  $\mathbb{N}^w(s)$ .

In the conditional segmentation probability  $P(I|L)$ , pixels in the object and background are supposed to follow Gaussian distributions. Thus, with different means  $\mu_{L_s}$  and standard deviations  $\sigma_{L_s}$ , the formula of  $P(I|L)$  is denoted by

$$P(I|L) = \prod_{s \in S} \frac{1}{\sqrt{2\pi}\sigma_{L_s}} \exp\left(-\frac{(I_s - \mu_{L_s})^2}{2\sigma_{L_s}^2}\right), \quad (13)$$

where  $\mu_{L_s}$  and  $\sigma_{L_s}$  are the mean and standard deviation of pixel intensity in the object or background, respectively, i.e.,

$$\begin{cases} \mu_{O_s} = \text{average}(I_s) \text{ in } \{\phi \geq 0\} \\ \mu_{B_s} = \text{average}(I_s) \text{ in } \{\phi < 0\}, \\ \sigma_{O_s} = \text{deviation}(I_s) \text{ in } \{\phi \geq 0\} \\ \sigma_{B_s} = \text{deviation}(I_s) \text{ in } \{\phi < 0\}. \end{cases} \quad (14)$$

where  $\mu_{O_s}$  and  $\mu_{B_s}$  are the mean pixel intensity in the object ( $O$ ) and background ( $B$ ), respectively;  $\sigma_{O_s}$  and  $\sigma_{B_s}$  are the standard deviation of pixel intensity in the object ( $O$ ) and background ( $B$ ), respectively.

In the prior segmentation probability  $P(L)$ , we assume that the label field knowledge  $P(L)$  of a pixel is only correlated with its neighborhood  $\mathbb{N}^w(s)$ , which is in accordance with the Markov property. As a result,  $P(L)$  can be represented as a Gibbs density according to the Hammersley-Clifford theorem [34], i.e.,

$$P(L) = \prod_{s \in S} \frac{1}{Z} \exp\left(-\sum_{c \in \mathbb{N}^w(s)} V_c(L_s)\right), \quad (15)$$

where  $Z$  is a normalizing constant,  $c$  is the set of all possible cliques, and  $V_c(L_s)$  is the clique energy function which is defined as

$$V_c(L_s) = \begin{cases} -\beta \left( \exp\left(-|I_s - I_{n(s)}|\right) \right), & L_s = L_{n(s)} \\ +\beta \left( \frac{2}{1+\exp(-|I_s - I_{n(s)}|)} - 1 \right), & L_s \neq L_{n(s)}, \end{cases} \quad (16)$$

where  $n(s) \in \mathbb{N}^w(s)$ ,  $|I_s - I_{n(s)}|$  is the absolute difference of intensities between the center pixel and one of its eight neighbors, and  $\beta$  is the Gibbsian parameter which is often set to an appropriately constant.

The above representation of  $P(L)$  shows that a pixel is regarded as the same label (object or background) as most of its neighbors. The more neighbors that have the same label as the center pixel, the more the  $P(L)$  is increased. In addition, the proposed clique energy function  $V_c(L_s)$  involves the intensity information of the image, which makes the prior segmentation probability  $P(L)$  adaptive to the local intensity.

Since an MAP problem is equivalent to an energy minimization problem, the energy equation of *a posteriori* segmentation probability  $P(L|I)$  can be rewritten as

$$\begin{aligned} En(L|I) &= -\log P(L|I) \approx -\log(P(L)P(I|L)) \\ &\approx \sum_{s \in S} \left( \frac{(I_s - \mu_{L_s})^2}{2\sigma_{L_s}^2} + \log(\sqrt{2\pi} Z \sigma_{L_s}) \right. \\ &\quad \left. + \sum_{c \in \mathbb{N}^w(s)} V_c(L_s) \right). \end{aligned} \quad (17)$$

By using the object *a posteriori* segmentation energy  $En(O|I)$  and the background *a posteriori* segmentation energy  $En(B|I)$ , our MRF energy function is defined as

$$E_{MRF} = En(O|I)H(\phi) + En(B|I)(1 - H(\phi)), \quad (18)$$

where  $H(\phi)$  is the Heaviside function which often used in a slightly smoothed form in practice, i.e.,

$$H_\varepsilon(\phi) = \begin{cases} 1, & \phi > \varepsilon \\ 0, & \phi < -\varepsilon \\ \frac{1}{2}(1 + \frac{\phi}{\varepsilon} + \frac{1}{\pi}\sin(\frac{\pi\phi}{\varepsilon})), & |\phi| \leq \varepsilon, \end{cases} \quad (19)$$

where  $\varepsilon$  is set to 1.5 for all experiments in this paper.

According to (3) and (9), the level set equation can then be written as

$$\frac{\partial \phi}{\partial t} = -\frac{\partial E}{\partial \phi} = T_{internal} + T_{external} + T_{MRF}, \quad (20)$$

where  $T_{internal}$  and  $T_{external}$  are the corresponding internal term and external term in the level set equation.  $T_{MRF}$  is the MRF term derived from the MRF energy function (18), i.e.,

$$T_{MRF} = -\delta(\phi)(En(O|I) - En(B|I)), \quad (21)$$

where  $\delta(\phi)$  is the Dirac function with the following smoothed form

$$\delta_\varepsilon(\phi) = \begin{cases} 0, & |\phi| > \varepsilon \\ \frac{1}{2\varepsilon}(1 + \cos(\frac{\pi\phi}{\varepsilon})), & |\phi| \leq \varepsilon. \end{cases} \quad (22)$$

In practice,  $T_{internal}$  and  $T_{external}$  can be designed based on different purposes. In this paper, we utilize the curvature of the evolving contour as the internal term, and adopt Li's penalty term for avoiding the re-initialization procedure [8] as the external term, i.e.,

$$\begin{aligned} T_{internal} &= \lambda |\nabla \phi| \operatorname{div} g\left(\frac{\nabla \phi}{|\nabla \phi|}\right), \\ T_{external} &= \gamma [\Delta \phi - \operatorname{div}\left(\frac{\nabla \phi}{|\nabla \phi|}\right)], \end{aligned} \quad (23)$$

where  $\lambda$  and  $\gamma$  are positive weighting constants.

The level set function  $\phi$  is initialized by the information of the initial contour  $C^0$ , i.e.,

$$\phi(x, y)^0 = \begin{cases} d, & (x, y) \in in(C^0) \\ 0, & (x, y) \in C^0 \\ -d, & (x, y) \in out(C^0), \end{cases} \quad (24)$$

where  $d$  is a positive constant (set to 5 in this paper).

There are several parameters affecting the segmentation performance in the proposed MRF embedded level set model, including the parameter  $w$  which controls the size of the neighborhood, the Gibbsian parameter  $\beta$ , and the parameters  $\lambda$  and  $\gamma$  determining the weight of internal term and external term in the energy function framework. Fig. 2 shows the segmentation results using different values of  $w$ ,  $\beta$ ,  $\lambda$  and  $\gamma$ , where the test images are taken from ETHZ database [35]. By comparing the results, we can draw the following conclusions: 1) when the parameter  $w$  is low, noise is easy to be treated as objects. Along with the increase of  $w$ , the segmented object boundary is more smooth at the cost of losing substantial details. To achieve a high accuracy, parameter  $w$  is set to 5 in the following experiments; 2) a low value of the parameter  $\beta$  may lead to the occurrence of weak boundary leakage, while a high value of  $\beta$  would prevent the evolving contour reaching

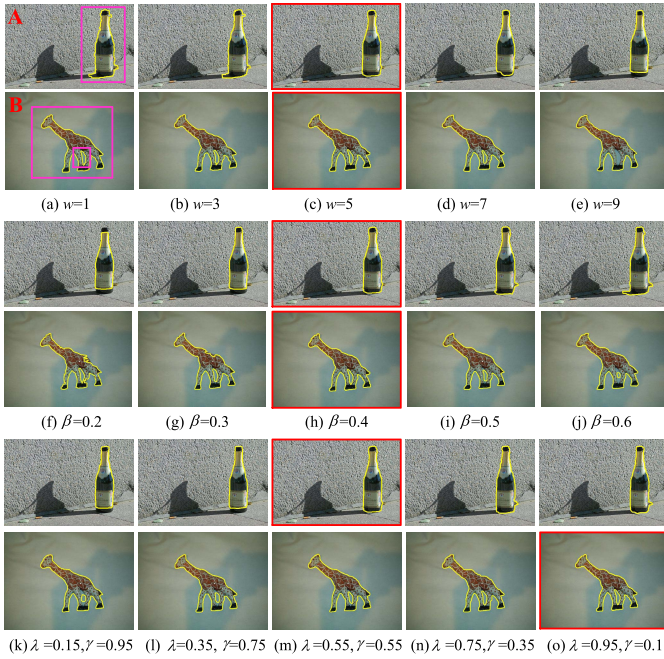


Fig. 2. Influence of different parameters on segmentation performance. (a)-(e) Segmentation results using different values of  $w$ ; (f)-(j) Segmentation results using different values of  $\beta$ ; (k)-(o) Segmentation results using different values of  $\lambda$  and  $\gamma$ . The initialization curve is marked in peach, and the final segmented object boundary is marked in yellow. We label the best segmentation results by red solid bounding box.

the real object boundary. To make a trade-off between miss segmentation and false segmentation, we set  $\beta$  to 0.4; and 3) the suitable choices of parameters  $\lambda$  and  $\gamma$  vary according to different images. In general, object with rough boundary (e.g., image B in Fig. 2) needs a high value of  $\lambda$  to strengthen the direction control of the evolving contour, while objects with smooth boundary (e.g., image A in Fig. 2) requires a relative high value of  $\gamma$ .

The model proposed by Darolli *et al.* [36] and our model exploit the MRF information under the level set paradigm differently in terms of the following three aspects: 1) Darolli *et al.* [36] leveraged the MRF information to refine the traditional region-based level set equation, which neither explores the related edge information nor deploys important regularization terms. By contrast, our model regards the proposed MRF energy function as a single term  $E_{MRF}$  and uses it to build a general energy function framework  $E = E_{internal} + E_{external} + E_{MRF}$ . The internal term  $E_{internal}$  and external term  $E_{external}$  can be designed for different purposes, and thus the related edge information and regularization terms can be duly considered; 2) The clique energy [36] used in MRF equation only considers the number of neighbor pixels which have the same (or different) label with the center pixel, while our model leverages the intensity information of neighbor pixels by a nonlinear function. Compared to [36], our model is adaptive to the local intensity, making the results more accurate and in line with the actual situation; and 3) the cost function of [36] is an approximation of our energy equation (17). The lack of term  $\log(\sqrt{2\pi} Z \sigma_{L_s})$  in [36] inevitably makes its accuracy lower than the proposed method. The implementations of the two models are different. In particular,

the proposed fast implementation is new and more efficient. Darolli *et al.* [36] exploited the integral sparse filed numeric algorithm [37] to reduce the size of the computation domain, while we integrated AMG to increase the time step and Li's penalty term to avoid the re-initialization procedure. Together with the technique of SFM, the proposed implementation is more efficient than that of [36] due to a much larger time step and a similar size of the computation domain. Additionally, the integral numeric algorithm in [36] is not accurate as the floating numeric algorithm in our implementation.

#### IV. NUMERICAL IMPLEMENTATION

This section explores AMG and SFM to obtain an efficient implementation of the MRF embedded level set model. In particular, AMG is able to increase the time step and SFM decreases the computation domain.

##### A. Algebraic Multigrid Based Numerical Scheme

The upwind scheme and the finite difference scheme for implementing level set models must satisfy the CFL condition [30], which leads to the need for a very small time step to avoid instability. We adopt a multiple scale based partial differential equation (PDE) solver, named algebraic multigrid (AMG) [32] to overcome this problem and speed up the computation.

According to the finite difference scheme (7), we can obtain the general discretization formula in a matrix-vector form

$$(\phi^{k+1} - \phi^k) / \Delta t = L\phi^k + F(\phi^k), \quad (25)$$

where  $L\phi^k = T_{internal}$ ,  $F(\phi^k) = T_{external} + T_{MRF}$ .

Specifically, due to the external term adopted from Li *et al.* [8], the signed distance property  $|\nabla\phi| = 1$  [7] can be maintained, especially in a neighborhood around the zero level set. Thus, the internal term  $T_{internal} = \lambda |\nabla\phi| \operatorname{div} g \left( \frac{\nabla\phi}{|\nabla\phi|} \right)$  can be simplified as  $\lambda \operatorname{div}(g \nabla\phi)$  and further approximated by the central difference as

$$\begin{aligned} \lambda \operatorname{div}(g \nabla\phi) &= \lambda(g\phi_x)_x + \lambda(g\phi_y)_y \\ &\approx \lambda/h_x^2 \{g_{i+1/2,j}(\phi_{i+1,j} - \phi_{i,j}) \\ &\quad - g_{i-1/2,j}(\phi_{i,j} - \phi_{i-1,j})\} \\ &\quad + \lambda/h_y^2 \{g_{i,j+1/2}(\phi_{i,j+1} - \phi_{i,j}) \\ &\quad - g_{i,j-1/2}(\phi_{i,j} - \phi_{i,j-1})\}, \end{aligned} \quad (26)$$

where  $h_x$  and  $h_y$  are the spatial finite difference discretization mesh grid lengths and is set as  $h_x = h_y = h$  here. A linear approximation for  $g$  is also made as  $g_{i+1/2,j} \approx (g_{i+1,j} + g_{i,j})/2$ . After scan the pixels in a row-major order, we can produce  $L = [l_{i,j}]$ , which is a  $N \times N$  ( $N = N_x N_y$  is pixel number of the image) matrix with elements as

$$l_{i,j} = \begin{cases} (g_i + g_j)/2h^2, & j \in (i) \\ -\sum_{k \in (i)} \frac{g_k + g_i}{2h^2}, & j = i \\ 0, & otherwise. \end{cases} \quad (27)$$

Although (25) is simple and explicit, the CFL condition [30] constrains its time step  $\Delta t$ .

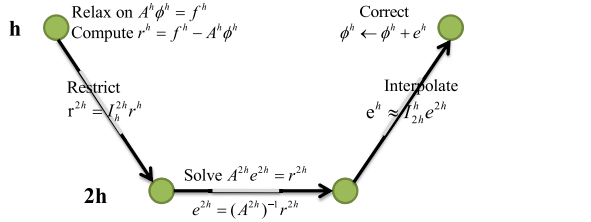


Fig. 3. The generic two-level multigrid of our linear system.

In this paper, we adopt the semi-implicit scheme [38] and obtain

$$(\phi^{k+1} - \phi^k)/\Delta t = L\phi^{k+1} + F(\phi^k). \quad (28)$$

This strategy is stable no matter how large the  $\Delta t$  is.

For each iteration, it is necessary to solve the following linear system

$$\left(\frac{1}{\Delta t}I - L\right)\phi^{k+1} = A\phi^{k+1} = \frac{1}{\Delta t}\phi^k + F(\phi^k) = f, \quad (29)$$

where  $A = (1/\Delta t)I - L$  is the system matrix which is very large for computation, and  $f$  is a known value at the iteration  $k$ . Therefore, the above expression can be simplified as

$$A\phi = f. \quad (30)$$

To solve this big linear system problem, simple iterative methods, e.g. Jacobi and Gauss-Seidel methods are inefficient. They suppress the low frequency part of the error slowly. Although their speed may be high at first, it becomes slow with the increase in iterations.

We thus use AMG to solve (30), because it is capable of solving a big linear system in an efficient way. AMG is a type of multigrid method [39] and is applied with the processes of smoothing and coarse grid correction. The smoothing process eliminates the high frequency error and the coarse grid correction reduces low frequency error, and thus the two operations significantly improve the convergence rate.

In particular, AMG does not require explicit knowledge of the problem's geometry, so it is convenient to implement AMG for the proposed MRF embedded level set model. Fig. 3 shows the generic two-level multigrid according to the linear system (30) of the proposed method, where  $I_h^{2h}$  and  $I_{2h}^h$  are the restriction operator and interpolation operator, respectively. We first input the system matrix corresponding to the finest grid  $A^h$ . Then, matrices for the coarser grid  $A^{2h}$  and the intergrid transfer operators  $I_h^{2h}$  and  $I_{2h}^h$  are computed automatically. Finally, the level set function  $\phi$  is updated through the correction procedure.

Since AMG allows large time step and is quick to suppress errors in both high and low frequencies, it needs only a few iterations to convergence. Another advantage of AMG is that it can be operated in a parallel fashion, e.g. on GPU [40], for handling large scale problems [41].

### B. Sparse Field Method Based Computation

Most existing level set methods update the level set function  $\phi$  in the full image domain, which makes them not

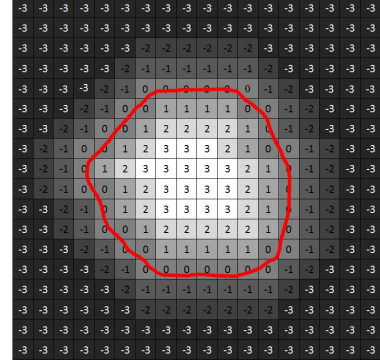


Fig. 4. An example of initialization in SFM.

applicable in large scale practical problems [42]. Narrow band methods [43] overcome this shortcoming by only updating points near the evolving contour. SFM [33] exploits this strategy to the extreme by setting the narrow band only one point wide; and hence, the calculated amount increases with the size of the curve length, rather than the resolution of the image.

The SFM uses five lists  $\{L_{-2}, L_{-1}, L_0, L_1, L_2\}$  to represent five different levels of an image, where the level information is determined by the value of the level set function  $\phi$ . We use two arrays to save the information of these lists. One is the  $\phi$  array which is saved at full floating point precision, and the other is a label map array with the values  $\{-3, -2, -1, 0, 1, 2, 3\}$  which is used to record the status of each point.

The procedure of SFM can be divided into two stages: initialization and contour evolution. Fig. 4 shows an example of the initialization of SFM. In the contour evolution stage, the changing status of  $L_0$  is determined by the AMG iteration. Then, by combining the neighborhood information, the changing status of points around  $L_0$  can be inferred and saved in five new lists  $\{S_{-2}, S_{-1}, S_0, S_1, S_2\}$ . Finally, points in the new lists change their status and one contour evolution is completed.

It is worth noting that the necessary input of SFM in the proposed method is the updated level set function of points in  $L_0$  which is only one point wide. This information is obtained by solving  $\phi^{k+1}$  in (30) via the AMG operation. Thus, the amount of calculation is significantly reduced.

The data structures used in SFM can perform in many parallel implementations, such as GPU [33], with ease, which creates the condition for further acceleration.

### C. Algorithm of the Proposed Method

A brief outline of the steps involved in the proposed fast and robust level set method is given in Algorithm 1.

Especially, the proposed efficient algorithm analyzes the reasons of high computational complexity in traditional methods, and resolves them by exploring the AMG and SFM. For the problem of restricted time step caused by the CFL condition [30], we derive the corresponding linear system formula of the proposed level set equation and utilize the AMG to solve it. Since the AMG has no constraint on the time step, it needs only a few iterations to convergence. For the problem of full domain computation (the level set functions of all the image pixels are updated in each iteration),

---

**Algorithm 1** Fast and Robust Level Set Method
 

---

**Step1: Initialization**

- 1) Initialize the level set function  $\phi$  according to (24).
- 2) Determine the image label map array by using the SFM initialization.

**Step 2: Update the zero level set**

- 1) Input  $\phi^k$  and  $f$  of the zero level set according to (29).
- 2) Compute the system matrix  $A$ .
- 3) Compute  $\phi^{k+1}$  by solving (30) through AMG.
- 4) Update the label map of zero level set according to  $\phi^{k+1}$ .

**Step 3: Update the narrow band**

- 1) Update other points in the narrow band through the SFM contour evolution.
  - 2) Go to step 2 until convergence.
- 

we employ the SFM technique and detail its processing procedure for the proposed MRF embedded level set. As a result, the computational domain is decreased to a narrow band which is only one point width (only level set functions of the pixels in the evolving contour are updated in each iteration). Moreover, both AMG and SFM have the parallel processing capability, which creates the opportunity for further acceleration.

In particular, for an image with  $N$  pixels, since the proposed method needs only a few iterations (less than  $\sqrt{N}$ ) to convergence through AMG, and for each iteration, only a small number (equivalent to the contour length (less than  $4\sqrt{N}$  for a square image)) of pixels are computed through SFM, the computational complexity of the proposed method is  $\sqrt{N} \times 4\sqrt{N} = O(N)$ . Compared with the  $O(N^2)$  complexity in traditional level set methods, our method is superior in terms of runtime. Additionally, the time cost of our combined AMG and SFM is definitely much shorter than previous papers [32], [33] using either of them.

## V. EXPERIMENTAL RESULTS

The performance of the proposed method has been validated in image segmentation experiments on a wide variety of images, including noisy synthetic images, SAR images, medical images and natural images. All experiments are performed on MATLAB R2010b installed in a computer with a 3.30GHz Intel Core i3 CPU and 4GB of RAM. The reference methods are GAC [6], DAC [9], CV [14], LBF [15], AMP [16], TCF [17], GM [25], TS [26] and GC [27], briefed in the Introduction section. Note the comparison methods and our method are pure data-driven and do not take the advantages of the shape priors. To conduct a fair comparison, we use the same initialization curve in both the reference methods and the proposed method. Also, the parameters of the reference methods are selected according to the values provided in the respective papers.

### A. Noisy Synthetic Image Segmentation

To test the robustness of the proposed method against noise, we independently add three kinds of noise (salt and pepper noise, Gaussian noise and speckle noise) to a synthetic image of size  $114 \times 101$  (shown in the first subfigure of Fig. 5). We select the following parameters for the proposed method:

$\lambda = 0.95$  (a relative high weight of the internal term is chosen due to the strong curvature change of the test images),  $\gamma = 0.25$ ,  $\Delta t = 30$ .

Fig. 5 shows binary segmentation results using different methods for the noisy synthetic images which added salt and pepper noise with increasing density. In this experiment, segmentation accuracy is measured by the percentage of pixels which are correctly classified, while the execution time is used for accurate and practical representation of segmentation speed. The curves of the segmentation accuracy and speed versus the density or variance of the above three kinds of noise using different methods are shown in Fig. 6.

It can be seen that compared with GAC, DAC, CV, LBF, AMP and GC, the superiority of the proposed method is significant in terms of segmentation accuracy and speed. Although the TCF algorithm achieves a comparable segmentation speed due to its simple operations between two linked lists and the Gaussian filtering process, the segmentation accuracy of TCF is lower than our method due to the ignorance of the relationship between pixels and their neighbors. Because the optimization schemes of GM and TS can avoid the segmentation results getting stuck in local minima, their segmentation accuracy is as high as our method. Meanwhile, TS needs much more time to segment a test image while GM achieves a comparable segmentation speed.

### B. SAR Image Segmentation

The segmentation of an SAR image [44], [45] is difficult because of its strong speckle noise. To test the robustness of our method against real noise, we conduct segmentation experiments on SAR images, including some simple images with a single target and some complex images with multiple targets. In this experiment,  $\lambda = 0.65$ ,  $\gamma = 0.25$ ,  $\Delta t = 35$ .

Fig. 7 compares results of segmentation on SAR images with different methods, which indicates that GM, TS and our method are much more robust against noise than other methods, and our method can preserve more details compared with GM and TS. Except the above visual evaluation, we also utilize a quantitative evaluation method, called texture-contrast locally weighted Mumford-Shah criterion (TLWM) [46], to measure the segmentation accuracy in absence of ground-truth data. The TLWM is defined as

$$D_{\{R_i\}}(F, \bar{F}) = \text{var}(F) = \sum_{i=1}^k \frac{1}{|R_i|} \sum_{(x,y) \in R_i} (F(x, y) - \bar{F}_i)^2, \quad (31)$$

where  $R_i$ ,  $i = 1, \dots, K$  are the disjoint regions in the segmented image;  $|R_i|$  is the area of the region (in pixels);  $F(x, y)$  is a certain feature of the input image, such as the contrast or texture transformations, and we use the pixel intensity in this paper;  $\bar{F}_i$  is the mean value of  $F(x, y)$  in each  $R_i$ . Actually, the TLWM measures the variance of disjoint regions in the segmentation result, and the lower the variance value  $\text{var}(F)$ , the better the segmentation result. Table I shows the TLWM results using different methods, which indicates that the proposed method hold the highest accuracy.

Table II gives the execution time of the above experiments, from which we can see that our method still keeps the

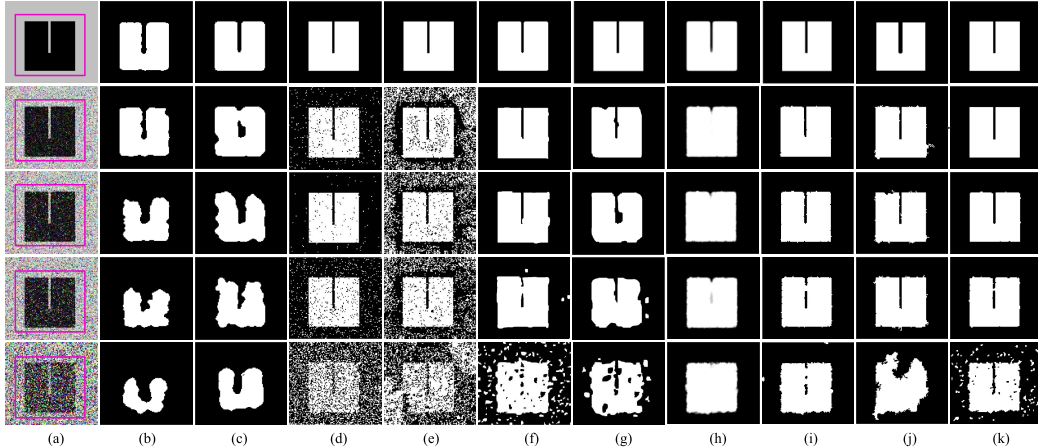


Fig. 5. Binary segmentation results using different methods for the noisy synthetic images with added salt and pepper noise and increasing density. (a) Original image with the initialization curve; (b) GAC; (c) DAC; (d) CV; (e) LBF; (f) AMP; (g) TCF; (h) GM; (i) TS; (j) GC; (k) Our method. Rows from top to bottom are the results for images which added salt and pepper noise with density 0, 0.01, 0.05, 0.1 and 0.5, respectively.

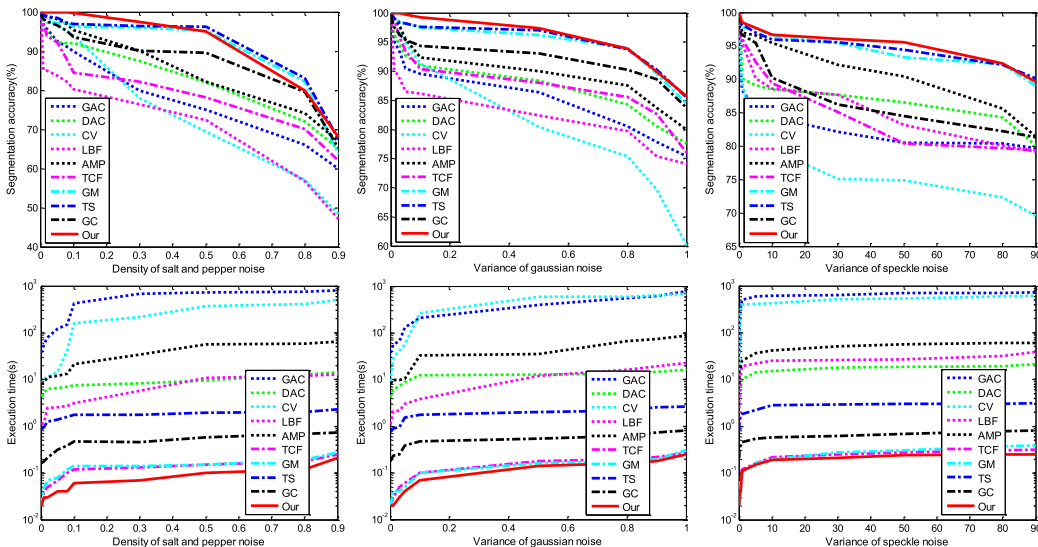


Fig. 6. Curves of the segmentation accuracy and speed versus the density or variance of three kinds of noise using different methods. The top row shows the curves of segmentation accuracy, the bottom row shows the curves of segmentation speed.

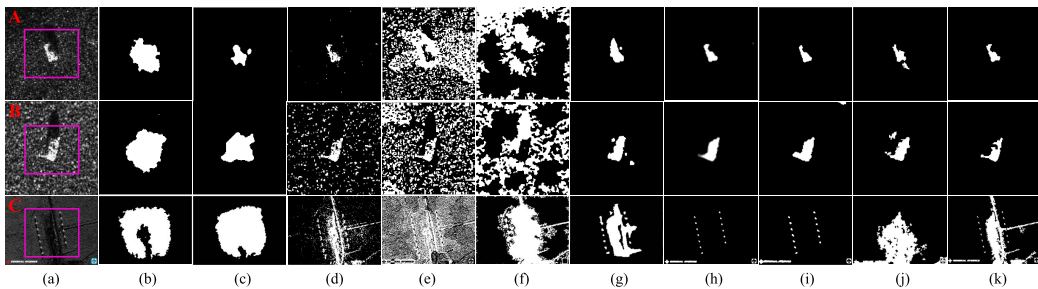


Fig. 7. Comparison results of segmentation of SAR images with different methods. (a) Original image with the initialization curve; (b) GAC; (c) DAC; (d) CV; (e) LBF; (f) AMP; (g) TCF; (h) GM; (i) TS; (j) GC; (k) Our method. Image A and B are single target images of sizes  $172 \times 173$  and  $128 \times 128$ , respectively; Image C is a multiple target image of size  $600 \times 438$ .

fastest segmentation speed and is much faster than GAC, DAC, CV, LBF, AMP, TS and GC. Note that TCF and GM achieve comparable segmentation speeds due to their fast implementations.

#### C. Medical Image Segmentation

Medical image segmentation [47], [48] plays an important role in computer aided diagnosis, such as segmenting the tumor tissues from the computed tomography (CT) image

of brain. However, medical image segmentation also has the problem of noise interference. The following parameters  $\lambda = 0.45$ ,  $\gamma = 0.30$ ,  $\Delta t = 35$  are set in this section.

We perform different methods on some CT images (of size  $416 \times 512$ ) of brain with kinds of tumor tissues. The compared segmentation results are shown in Fig. 8, and the corresponding segmentation accuracy measured by TLWM is given in Table III. Table IV gives the comparison

TABLE I  
COMPARISON OF SEGMENTATION ACCURACY (VAR ( $F$ ) IN TLWN) WITH DIFFERENT METHODS IN SAR IMAGE SEGMENTATION

Image	GAC	DAC	CV	LBF	AMP	TCF	GM	TS	GC	Our
A	0.486	0.201	0.139	0.664	0.712	0.186	0.061	0.063	0.116	<b>0.058</b>
B	0.669	0.270	0.203	0.319	0.738	0.197	0.059	0.062	0.189	<b>0.060</b>
C	0.871	0.912	0.352	0.732	0.773	0.205	0.132	0.145	0.509	<b>0.108</b>

TABLE II  
COMPARISON OF EXECUTION TIME WITH DIFFERENT METHODS IN SAR IMAGE SEGMENTATION (SECONDS)

Image	GAC	DAC	CV	LBF	AMP	TCF	GM	TS	GC	Our
A	45.32	5.92	20.15	6.54	18.12	2.14	1.12	4.52	3.24	<b>1.09</b>
B	50.76	6.32	19.63	5.98	13.56	1.15	1.10	5.26	3.18	<b>1.08</b>
C	399.22	22.91	105.63	35.10	79.19	7.88	7.53	10.32	9.24	<b>7.65</b>

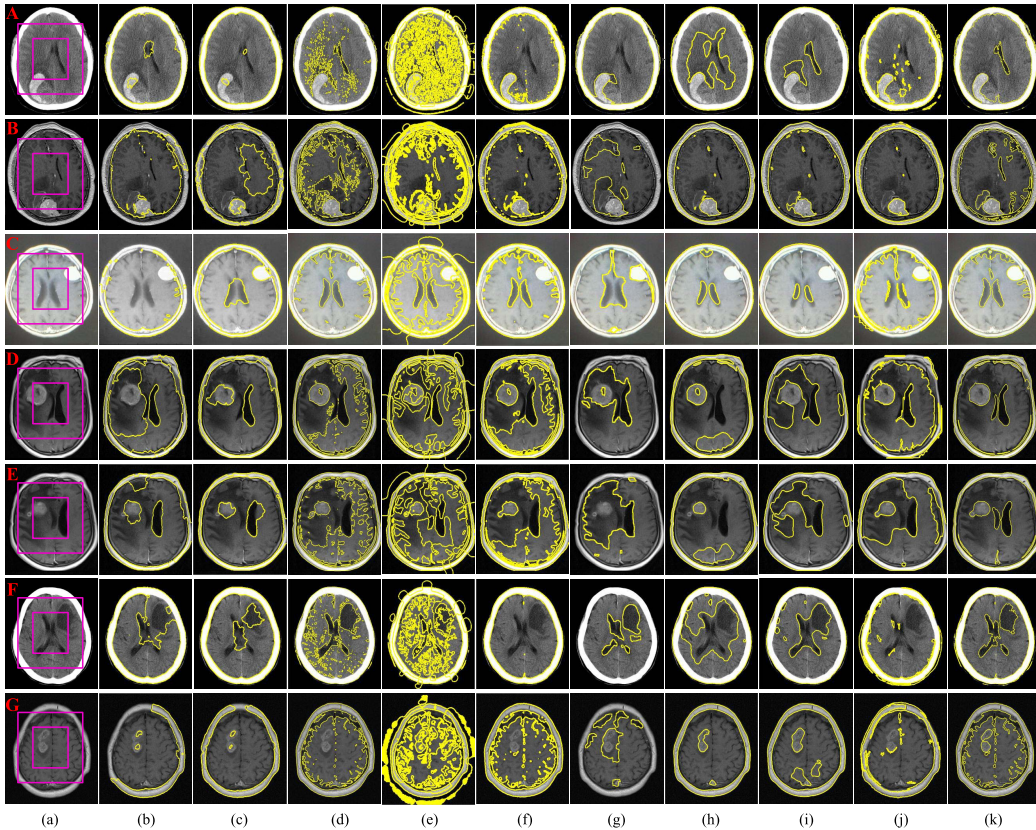


Fig. 8. Compared segmentation results of medical images with different methods. (a) Original image with the initialization curve; (b) GAC; (c) DAC; (d) CV; (e) LBF; (f) AMP; (g) TCF; (h) GM; (i) TS; (j) GC; (k) Our method. Image A and B are CT images of brain with fibroma; Image C, D and E are CT images of brain with meningioma; Image F and G are CT images of brain with glioma.

of their execution time. From the segmentation results, we can conclude that not as other methods missing the tumor tissues or containing much noise, our method can segment most of the tumor tissues with low noise interference. Meanwhile, the speed of our method is also among the fastest.

#### D. Natural Image Segmentation

The natural images used in this experiment are taken from BSDS500 [49], ETHZ [35] and Weizmann [50] databases. Segmentation accuracy is measured by the *precision* and

*recall* [51] of the information of ground-truth provided by these databases. In this experiment,  $\lambda = 0.65$ ,  $\gamma = 0.25$ ,  $\Delta t = 20$  (a relative small time step is set because of the complex background of natural images).

Fig. 9 compares results of natural image segmentation with different methods. For images with multiple objects (Images F and G), the proposed method simply treats different objects as foreground, and conducts two-phase segmentation to separate this foreground from the background. Tables V and VI compare the segmentation accuracy and speed of different methods, respectively.

TABLE III  
COMPARISON OF SEGMENTATION ACCURACY (VAR ( $F$ ) IN TLWN) WITH DIFFERENT METHODS IN MEDICAL IMAGE SEGMENTATION

Image	GAC	DAC	CV	LBF	AMP	TCF	GM	TS	GC	Our
A	0.076	0.031	0.134	0.476	0.187	0.108	0.125	0.084	0.067	<b>0.026</b>
B	0.431	0.229	0.512	0.661	0.176	0.329	0.115	0.101	0.094	<b>0.087</b>
C	0.167	0.109	0.208	0.886	0.309	0.121	0.111	0.129	0.214	<b>0.091</b>
D	0.341	0.187	0.480	0.719	0.553	0.247	0.258	0.247	0.301	<b>0.096</b>
E	0.198	0.097	0.329	0.651	0.592	0.345	0.203	0.227	0.319	<b>0.079</b>
F	0.380	0.175	0.307	0.619	0.176	0.102	0.308	0.157	0.268	<b>0.084</b>
G	0.109	0.092	0.341	0.871	0.337	0.219	0.196	0.221	0.335	<b>0.076</b>

TABLE IV  
COMPARISON OF EXECUTION TIME WITH DIFFERENT METHODS IN MEDICAL IMAGE SEGMENTATION (SECONDS)

Image	GAC	DAC	CV	LBF	AMP	TCF	GM	TS	GC	Our
A	98.36	6.63	69.35	5.28	16.99	2.01	1.62	4.68	3.24	<b>1.21</b>
B	118.29	5.98	54.13	5.03	15.29	1.88	0.96	3.15	2.54	<b>1.09</b>
C	159.65	9.62	115.36	16.32	26.76	3.81	2.44	5.31	4.19	<b>2.32</b>
D	105.98	8.17	86.53	8.25	12.43	3.29	1.35	5.62	3.36	<b>1.19</b>
E	289.27	10.26	124.25	19.63	31.52	5.60	2.87	6.84	4.06	<b>3.32</b>
F	203.46	12.65	98.15	9.53	25.46	2.56	2.40	5.28	3.11	<b>2.36</b>
G	99.35	9.67	76.54	6.91	19.62	3.49	1.90	4.21	3.98	<b>2.13</b>

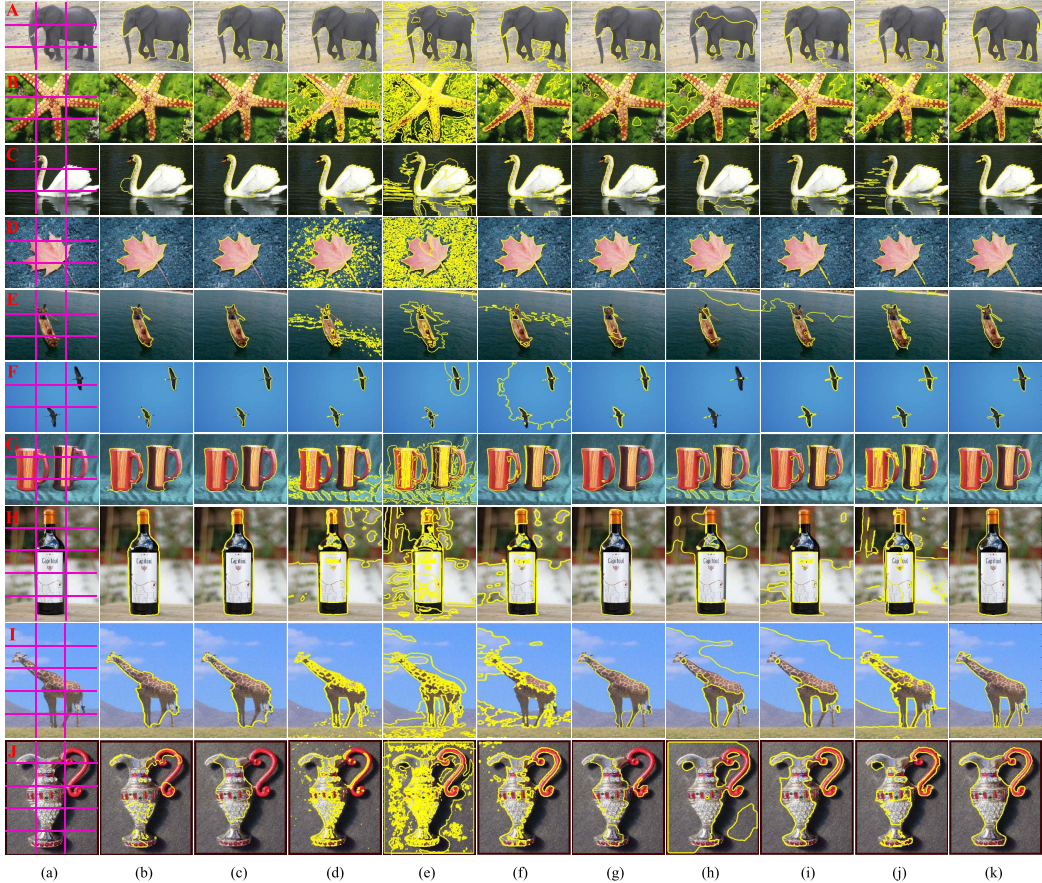


Fig. 9. Compared segmentation results of natural images with different methods. (a) Original image with the initialization curve; (b) GAC; (c) DAC; (d) CV; (e) LBF; (f) AMP; (g) TCF; (h) GM; (i) TS; (j) GC; (k) Our method. The image size of A, B, C, D, E, F, G, H, I and J are  $300 \times 225$ ,  $481 \times 321$ ,  $481 \times 321$ ,  $300 \times 203$ ,  $300 \times 226$ ,  $300 \times 248$ ,  $509 \times 398$ ,  $340 \times 490$ ,  $280 \times 500$  and  $226 \times 300$ , respectively.

From these comparison results, we have the following conclusions. Firstly, our method can segment objects from a background with relatively accurate shapes. Secondly, the precision and recall of our method is higher than those obtained

by other comparison baselines. Finally, the proposed method greatly improves the segmentation speed of methods GAC, DAC, CV, LBF, AMP, TS and GC, and still keeps comparable segmentation efficiency with these fast methods TCF can GM.

TABLE V

COMPARISON OF SEGMENTATION ACCURACY WITH DIFFERENT METHODS IN NATURAL IMAGE SEGMENTATION (PRECISION(%)/RECALL(%))

Image	GAC	DAC	CV	LBF	AMP	TCF	GM	TS	GC	Our
A	98.21/91.02	99.02/89.79	95.43/95.49	80.45/99.51	90.46/97.61	98.98/90.62	99.95/75.25	93.12/96.31	89.16/93.12	<b>99.89/99.91</b>
B	50.61/19.65	99.61/51.02	31.04/40.06	40.77/89.65	79.02/98.05	94.65/59.86	60.35/93.41	85.11/80.14	74.19/61.15	<b>95.43/99.87</b>
C	91.87/94.03	98.54/89.72	69.51/90.42	42.54/97.88	81.05/97.12	95.34/90.15	86.14/95.41	90.12/94.19	70.24/93.98	<b>99.66/98.54</b>
D	96.11/95.43	97.12/95.16	85.53/98.79	64.12/98.19	95.41/99.12	92.48/95.61	91.95/99.98	94.21/98.01	97.88/99.85	<b>98.96/99.98</b>
E	98.99/94.98	94.19/96.29	59.81/60.11	43.21/79.65	54.81/83.65	97.62/95.02	65.21/94.53	55.42/90.54	85.69/96.87	<b>99.15/99.28</b>
F	99.15/80.16	99.43/89.65	99.19/95.16	71.64/94.39	35.82/92.64	98.60/88.43	99.98/15.04	98.21/98.69	97.54/99.39	<b>98.11/99.91</b>
G	96.87/94.02	98.54/96.54	49.81/57.65	38.11/82.51	93.19/80.67	98.94/85.24	80.32/93.54	98.24/78.19	91.98/84.35	<b>99.15/98.16</b>
H	99.16/99.04	99.21/99.35	71.04/70.85	50.09/89.14	66.07/80.97	96.37/99.16	79.62/91.47	61.04/74.12	55.20/95.39	<b>99.24/99.05</b>
I	82.49/90.04	84.11/91.54	90.05/92.77	78.15/95.43	41.02/49.08	86.31/92.01	59.84/51.22	63.24/49.87	76.59/97.88	<b>96.81/98.54</b>
J	90.15/30.19	96.79/70.07	90.16/81.54	49.53/89.66	91.57/92.44	95.41/69.45	65.89/96.66	90.24/87.16	94.69/62.35	<b>97.15/99.16</b>

TABLE VI

COMPARISON OF EXECUTION TIME WITH DIFFERENT METHODS IN NATURAL IMAGE SEGMENTATION (SECONDS)

Image	GAC	DAC	CV	LBF	AMP	TCF	GM	TS	GC	Our
A	150.22	7.12	102.69	8.65	36.85	1.32	0.96	10.98	9.21	<b>1.15</b>
B	142.33	11.56	205.36	10.23	45.12	3.06	1.99	11.65	8.43	<b>2.33</b>
C	201.46	8.31	98.26	7.51	31.99	1.24	1.95	12.24	10.62	<b>1.19</b>
D	225.37	7.41	105.89	7.12	30.81	1.26	0.84	8.32	6.24	<b>1.11</b>
E	180.24	15.29	89.77	12.43	25.33	2.57	1.85	10.65	7.21	<b>2.14</b>
F	51.24	5.12	69.24	6.10	19.12	1.28	1.59	9.62	8.54	<b>1.06</b>
G	112.68	7.47	76.54	9.23	44.65	1.96	1.29	10.51	7.20	<b>1.10</b>
H	203.46	17.43	65.55	14.69	40.58	3.14	1.69	10.25	8.06	<b>2.25</b>
I	248.14	11.58	128.61	23.96	61.24	3.77	1.50	9.44	7.59	<b>2.32</b>
J	147.31	9.94	74.35	18.77	54.68	2.06	1.64	10.87	6.65	<b>1.29</b>



Fig. 10. Examples of undesirable segmentation results. Rows from top to bottom are segmentation results obtained by the proposed method, TCF and TS, respectively. All images are of the same size 481 × 321.

### E. Analysis of Undesirable Segmentation Results

In practice, the proposed method performs poorly when images exhibit complex backgrounds or blurry object boundaries. Fig. 10 shows examples of undesirable segmentation results using the proposed method, noting that the initialization and parameters of all images are set in the same way as those in Fig. 9. It can be seen that some segmented contours deviate from the real objects, while some segmented contours loss a lot of details.

The reasons leading to these failed segmentations are various. On one hand, there are a few difference approximations (e.g., central difference in (26)) in our numerical implementation to make processing simpler and faster. When the boundary of object and background is obscure, the difference approximations will inevitably introduce large error during the evolution. On the other hand, due to the internal term which aims to keep the smoothness of the evolving curve, some details near the boundary with high contrast are easy

to be omitted for avoiding the sharp shape of evolving curve. Additionally, the lack of prior information (e.g., overall shape of the object) creates difficulties in segmenting images with complex backgrounds.

We also select two methods (TCF and TS) which achieve high performance in the previous experiments to segment these challenging images. Results shown in Fig. 10 indicate that these two methods also fail to obtain correct object boundaries. It is worth noting that although the recent approach TS leverages related optimization scheme to avoid the local minima decreasing the segmentation accuracy, its optimization problem is the Mumford-Shah energy functional [19] which is the same as the CV model [14] lacking the capability for encoding the correlation between neighboring pixels. Thus, it is not robust enough against heavy noise in these challenging images.

In the future, we will consider solving these problems by exploiting the optimization schemes recent approaches (e.g., TS) used to solve the proposed MRF embedded energy

functional. Also, we will explore effective terms (e.g., shape constraints [52]) in the proposed energy framework and accurate yet fast numerical schemes for implementation.

## VI. CONCLUSIONS

In this paper, we develop a fast and robust level set method by embedding MRF energy function to the conventional level set function to suppress the effect of noise and exploring AMG and SFM to obtain an efficient implementation of the MRF embedded level set model. The proposed method has been applied to various kinds of images, including noisy synthetic images, SAR images, medical images and natural images. The experimental results show that our method can obtain robust segmentation results on noised images in a very short time. In addition, the parallel processing capability of our method makes it promising for the segmentation of big images.

## REFERENCES

- [1] J. Shen, Y. Du, W. Wang, and X. Li, "Lazy random walks for superpixel segmentation," *IEEE Trans. Image Process.*, vol. 23, no. 4, pp. 1451–1462, Apr. 2014.
- [2] X. Lu and X. Li, "Group sparse reconstruction for image segmentation," *Neurocomputing*, vol. 136, pp. 41–48, Jul. 2014.
- [3] S. Osher and J. A. Sethian, "Fronts propagating with curvature-dependent speed: Algorithms based on Hamilton–Jacobi formulations," *J. Comput. Phys.*, vol. 79, no. 1, pp. 12–49, Nov. 1988.
- [4] M. Kass, A. Witkin, and D. Terzopoulos, "Snakes: Active contour models," *Int. J. Comput. Vis.*, vol. 1, no. 4, pp. 321–331, Apr. 1988.
- [5] C. Xu and J. L. Prince, "Snakes, shapes, and gradient vector flow," *IEEE Trans. Image Process.*, vol. 7, no. 3, pp. 359–369, Mar. 1988.
- [6] V. Caselles, R. Kimmel, and G. Sapiro, "Geodesic active contours," *Int. J. Comput. Vis.*, vol. 22, no. 1, pp. 61–79, Jan. 1997.
- [7] R. Goldenberg, R. Kimmel, E. Rivlin, and M. Rudzsky, "Fast geodesic active contours," *IEEE Trans. Image Process.*, vol. 10, no. 10, pp. 1467–1475, Oct. 2001.
- [8] C. Li, C. Xu, C. Gui, and M. D. Fox, "Level set evolution without re-initialization: A new variational formulation," in *Proc. IEEE Comput. Soc. Conf. Comput. Vis. Pattern Recognit.*, Jun. 2005, pp. 430–436.
- [9] A. K. Mishra, P. W. Fieguth, and D. A. Clausi, "Decoupled active contour (DAC) for boundary detection," *IEEE Trans. Pattern Anal. Mach. Intell.*, vol. 33, no. 2, pp. 310–324, Feb. 2011.
- [10] B. Wang, X. Gao, D. Tao, and X. Li, "A nonlinear adaptive level set for image segmentation," *IEEE Trans. Cybern.*, vol. 44, no. 3, pp. 418–428, Mar. 2014.
- [11] X. Yang, X. Gao, J. Li, and B. Han, "A shape-initialized and intensity-adaptive level set method for auroral oval segmentation," *Inf. Sci.*, vol. 277, pp. 794–807, Sep. 2014.
- [12] X. Gao, B. Wang, D. Tao, and X. Li, "A relay level set method for automatic image segmentation," *IEEE Trans. Syst., Man, Cybern. B, Cybern.*, vol. 41, no. 2, pp. 518–525, Apr. 2011.
- [13] X. Yang, X. Gao, D. Tao, and X. Li, "Improving level set method for fast auroral oval segmentation," *IEEE Trans. Image Process.*, vol. 23, no. 7, pp. 2854–2865, Jul. 2014.
- [14] T. F. Chan and L. A. Vese, "Active contours without edges," *IEEE Trans. Image Process.*, vol. 10, no. 2, pp. 266–277, Feb. 2001.
- [15] C. Li, C.-Y. Kao, J. C. Gore, and Z. Ding, "Implicit active contours driven by local binary fitting energy," in *Proc. IEEE Conf. Comput. Vis. Pattern Recognit.*, Jun. 2007, pp. 1–7.
- [16] H. Wu, V. Appia, and A. Yezzi, "Numerical conditioning problems and solutions for nonparametric i.i.d. statistical active contours," *IEEE Trans. Pattern Anal. Mach. Intell.*, vol. 35, no. 6, pp. 1298–1311, Jun. 2013.
- [17] Y. Shi and W. C. Karl, "Real-time tracking using level sets," in *Proc. IEEE Comput. Soc. Conf. Comput. Vis. Pattern Recognit.*, Jun. 2005, pp. 20–25.
- [18] B. Wang, X. Gao, D. Tao, and X. Li, "A unified tensor level set for image segmentation," *IEEE Trans. Syst., Man, Cybern. B, Cybern.*, vol. 40, no. 3, pp. 857–867, Jun. 2010.
- [19] D. Mumford and J. Shah, "Boundary detection by minimizing functionals," in *Proc. IEEE Conf. Comput. Vis. Pattern Recognit.*, Jun. 1985, pp. 22–26.
- [20] Q. Huang, X. Bai, Y. Li, L. Jin, and X. Li, "Optimized graph-based segmentation for ultrasound images," *Neurocomputing*, vol. 129, pp. 216–224, Apr. 2014.
- [21] J. Shen, Y. Du, and X. Li, "Interactive segmentation using constrained Laplacian optimization," *IEEE Trans. Circuits Syst. Video Technol.*, vol. 24, no. 7, pp. 1088–1100, Jul. 2014.
- [22] K. Zhang, Q. Liu, H. Song, and X. Li, "A variational approach to simultaneous image segmentation and bias correction," *IEEE Early Access Article*, doi: 10.1109/TCYB.2014.2352343.
- [23] R. Hong, M. Wang, Y. Gao, D. Tao, X. Li, and X. Wu, "Image annotation by multiple-instance learning with discriminative feature mapping and selection," *IEEE Trans. Cybern.*, vol. 44, no. 5, pp. 669–680, May 2014.
- [24] H. Zhou, X. Li, G. Schaefer, M. E. Celebi, and P. Miller, "Mean shift based gradient vector flow for image segmentation," *Comput. Vis. Image Understand.*, vol. 117, no. 9, pp. 1004–1016, Sep. 2013.
- [25] T. F. Chan, S. Esedoglu, and M. Nikolova, "Algorithms for finding global minimizers of image segmentation and denoising models," *SIAM J. Appl. Math.*, vol. 66, no. 5, pp. 1632–1648, May 2006.
- [26] X. Cai, R. Chan, and T. Zeng, "A two-stage image segmentation method using a convex variant of the Mumford–Shah model and thresholding," *SIAM J. Imag. Sci.*, vol. 6, no. 1, pp. 368–390, Feb. 2013.
- [27] E. Bae and X.-C. Tai, "Graph cut optimization for the piecewise constant level set method applied to multiphase image segmentation," in *Proc. 2nd Int. Conf. Scale Space Variational Methods Comput. Vis.*, 2009, pp. 1–13.
- [28] L. Zheng, S. Wang, and Q. Tian, "Coupled binary embedding for large-scale image retrieval," *IEEE Trans. Image Process.*, vol. 23, no. 8, pp. 3368–3380, Aug. 2014.
- [29] Z. Liu, H. Li, L. Zhang, W. Zhou, and Q. Tian, "Cross-indexing of binary SIFT codes for large-scale image search," *IEEE Trans. Image Process.*, vol. 23, no. 5, pp. 2047–2057, May 2014.
- [30] J. Weickert, B. M. T. H. Romeny, and M. A. Viergever, "Efficient and reliable schemes for nonlinear diffusion filtering," *IEEE Trans. Image Process.*, vol. 7, no. 3, pp. 398–410, Mar. 1998.
- [31] D. Lin and J. Fisher, "Low level vision via switchable Markov random fields," in *Proc. IEEE Conf. Comput. Vis. Pattern Recognit.*, Jun. 2012, pp. 2432–2439.
- [32] D. Kushnir, M. Galun, and A. Brandt, "Efficient multilevel eigensolvers with applications to data analysis tasks," *IEEE Trans. Pattern Anal. Mach. Intell.*, vol. 32, no. 8, pp. 1377–1391, Aug. 2010.
- [33] A. C. Jalba, W. J. van der Laan, and J. B. T. M. Roerdink, "Fast sparse level sets on graphics hardware," *IEEE Trans. Vis. Comput. Graphics*, vol. 19, no. 1, pp. 30–44, Jan. 2013.
- [34] J. Besag, "Spatial interaction and the statistical analysis of lattice systems," *J. Roy. Statist. Soc., Ser. B*, vol. 36, no. 2, pp. 192–236, 1974.
- [35] V. Ferrari, F. Jurie, and C. Schmid, "From images to shape models for object detection," *Int. J. Comput. Vis.*, vol. 87, no. 3, pp. 284–303, Mar. 2010.
- [36] C. Darolli, A. Mertins, C. Bodensteiner, and U. G. Hofmann, "Local region descriptors for active contours evolution," *IEEE Trans. Image Process.*, vol. 17, no. 12, pp. 2275–2288, Dec. 2008.
- [37] Y. Shi and W. C. Karl, "A fast level set method without solving PDEs," in *Proc. IEEE Int. Conf. Acoust., Speech, Signal Process.*, Mar. 2005, pp. 97–100.
- [38] G. Papandreou and P. Maragos, "Multigrid geometric active contour models," *IEEE Trans. Image Process.*, vol. 16, no. 1, pp. 229–240, Jan. 2007.
- [39] S. T. Acton, "Multigrid anisotropic diffusion," *IEEE Trans. Image Process.*, vol. 7, no. 3, pp. 280–291, Mar. 1998.
- [40] J. Bolz, I. Farmer, E. Grinshpan, and P. Schröder, "Sparse matrix solvers on the GPU: Conjugate gradients and multigrid," *ACM Trans. Graph.*, vol. 22, no. 3, pp. 917–924, Jul. 2003.
- [41] L. Zheng, S. Wang, and Q. Tian, " $\mathcal{L}_p$ -norm IDF for scalable image retrieval," *IEEE Trans. Image Process.*, vol. 23, no. 8, pp. 3604–3617, Aug. 2014.
- [42] L. Zheng and S. Wang, "Visual phraselet: Refining spatial constraints for large scale image search," *IEEE Signal Process. Lett.*, vol. 20, no. 4, pp. 391–394, Apr. 2013.
- [43] D. Adalsteinsson and J. A. Sethian, "A fast level set method for propagating interfaces," *J. Comput. Phys.*, vol. 118, no. 2, pp. 269–277, May 1995.
- [44] R. C. P. Marques, F. N. Medeiros, and J. S. Nobre, "SAR image segmentation based on level set approach and  $\mathcal{G}_A^0$  model," *IEEE Trans. Pattern Anal. Mach. Intell.*, vol. 34, no. 10, pp. 2046–2057, Oct. 2012.
- [45] D. Yang, G. Liao, S. Zhu, X. Yang, and X. Zhang, "SAR imaging with

- undersampled data via matrix completion," *IEEE Geosci. Remote Sens. Lett.*, vol. 11, no. 9, pp. 1539–1543, Sep. 2014.
- [46] A. Sofou and P. Maragos, "Generalized flooding and multicue PDE-based image segmentation," *IEEE Trans. Image Process.*, vol. 17, no. 3, pp. 364–376, Mar. 2008.
- [47] P. Yan, W. Zhang, B. Turkbey, P. L. Choyke, and X. Li, "Global structure constrained local shape prior estimation for medical image segmentation," *Comput. Vis. Image Understand.*, vol. 117, no. 9, pp. 1017–1026, Sep. 2013.
- [48] M. Yang, X. Li, B. Turkbey, P. L. Choyke, and P. Yan, "Prostate segmentation in MR images using discriminant boundary features," *IEEE Trans. Biomed. Eng.*, vol. 60, no. 2, pp. 479–488, Feb. 2013.
- [49] P. Arbelaez, B. Hariharan, C. Gu, S. Gupta, L. Bourdev, and J. Malik, "Semantic segmentation using regions and parts," in *Proc. IEEE Conf. Comput. Vis. Pattern Recognit.*, Jun. 2012, pp. 3378–3385.
- [50] S. Alpert, M. Galun, R. Basri, and A. Brandt, "Image segmentation by probabilistic bottom-up aggregation and cue integration," in *Proc. IEEE Conf. Comput. Vis. Pattern Recognit.*, Jun. 2007, pp. 1–8.
- [51] F. J. Estrada and A. D. Jepson, "Benchmarking image segmentation algorithms," *Int. J. Comput. Vis.*, vol. 85, no. 2, pp. 167–181, Nov. 2009.
- [52] X. Qin, X. Li, Y. Liu, H. Lu, and P. Yan, "Adaptive shape prior constrained level sets for bladder MR image segmentation," *IEEE J. Biomed. Health Informat.*, vol. 18, no. 5, pp. 1707–1716, Sep. 2014.



**Xi Yang** received the B.Eng. degree in electronic information engineering from Xidian University, Xi'an, China, in 2010, where she is currently pursuing the Ph.D. degree in pattern recognition and intelligent system with the School of Electronic Engineering. From 2013 to 2014, she was a visiting Ph.D. student with the Department of Computer Science, University of Texas at San Antonio, San Antonio, TX, USA. Her current research interests include image/video processing, computer vision, and multimedia information retrieval.



**Xinbo Gao** (M'02–SM'07) received the B.Eng., M.Sc., and Ph.D. degrees in signal and information processing from Xidian University, Xi'an, China, in 1994, 1997, and 1999, respectively. From 1997 to 1998, he was a Research Fellow with the Department of Computer Science, Shizuoka University, Shizuoka, Japan. From 2000 to 2001, he was a Post-Doctoral Research Fellow with the Department of Information Engineering, Chinese University of Hong Kong, Hong Kong. Since 2001, he has been with the School of Electronic Engineering, Xidian University. He is currently a Cheung Kong Professor with the Ministry of Education, China, a Professor of Pattern Recognition and Intelligent System, and the Director of the State Key Laboratory of Integrated Services Networks. His research interests are computational intelligence, machine learning, computer vision, pattern recognition, and wireless communications. He has authored five books and around 200 technical articles in refereed journals and proceedings, including the *IEEE TRANSACTIONS ON IMAGE PROCESSING*, the *IEEE TRANSACTIONS ON NEURAL NETWORKS AND LEARNING SYSTEMS*, the *IEEE TRANSACTIONS ON SYSTEMS, MAN, AND CYBERNETICS*, the *IEEE TRANSACTIONS ON CIRCUITS AND SYSTEMS FOR VIDEO TECHNOLOGY*, the *International Journal of Computer Vision*, *Pattern Recognition* etc.. He is on the Editorial Boards of several journals, including *Signal Processing* (Elsevier), and *Neurocomputing* (Elsevier). He served as the General Chair/Co-Chair or Program Committee Chair/Co-Chair or Program Committee Member for around 30 major international conferences. He is a Fellow of the Institution of Engineering and Technology and Senior Member of the Institute of Electrical and Electronics Engineers.



**Dacheng Tao** (M'07–SM'12) is currently a Professor of Computer Science with the Centre for Quantum Computation & Intelligent Systems, and the Faculty of Engineering and Information Technology, University of Technology, Sydney. He mainly applies statistics and mathematics for data analytics. His research interests spread across computer vision, data mining, geoinformatics, image processing, machine learning, multimedia, and video surveillance. His research results have expounded in one monograph and over 100 publications at prestigious journals and prominent conferences, such as the *IEEE TRANSACTIONS ON PATTERN ANALYSIS AND MACHINE INTELLIGENCE*, the *IEEE TRANSACTIONS ON NEURAL NETWORKS AND LEARNING SYSTEMS*, the *IEEE TRANSACTIONS ON IMAGE PROCESSING*, the *IEEE TRANSACTIONS ON SIGNAL PROCESSING*, the *IEEE TRANSACTIONS ON KNOWLEDGE AND DATA ENGINEERING*, the *IEEE TRANSACTIONS ON CYBERNETICS*, the *Journal of Machine Learning Research*, the *International Journal of Computer Vision*, the Neural Information Processing Systems Conference, the International Conference on Machine Learning, the Conference on Computer Vision and Pattern Recognition, the International Conference on Computer Vision, the European Conference on Computer Vision, the International Conference on Artificial Intelligence and Statistics, the IEEE International Conference on Data Mining (ICDM), the ACM Special Interest Group on Knowledge Discovery and Data Mining, and the ACM Multimedia, with several best paper awards, such as the Best Theory/Algorithm Paper Runner Up Award in the IEEE ICDM'07 and the Best Student Paper Award in the IEEE ICDM'13.

**Xuelong Li** (M'02–SM'07–F'12) is currently a Full Professor with the Center for OPTical IMagery Analysis and Learning (OPTIMAL), State Key Laboratory of Transient Optics and Photonics, Xi'an Institute of Optics and Precision Mechanics, Chinese Academy of Sciences, Xi'an, China.



**Jie Li** received the B.Sc. degree in electronic engineering, the M.Sc. degree in signal and information processing, and the Ph.D. degree in circuit and systems from Xidian University, Xi'an, China, in 1995, 1998, and 2004, respectively, where she is currently a Professor with the School of Electronic Engineering. Her research interests include video processing and machine learning. She has authored around 50 technical articles in refereed journals and proceedings, including the *IEEE TRANSACTIONS ON IMAGE PROCESSING*, the *IEEE TRANSACTIONS ON CIRCUITS AND SYSTEMS FOR VIDEO TECHNOLOGY*, *Information Sciences* etc..